JOURNAL OF SOLID STATE CHEMISTRY 101, 1–17 (1992)

Structural Chemistry and Physical Properties of Some Ternary Oxides in the Bi_2O_3–Ta_2O_5 System

WUZONG ZHOU

IRC in Superconductivity, University of Cambridge, Madingley Road, Cambridge CB3 0HE, United Kingdom

Received November 14, 1991; in revised form February 24, 1992; accepted March 27, 1992

A high-resolution electron microscope has been used in structural investigation of the Bi_2O_3–Ta_2O_5 system. Several distinct phases in the compositional range between Bi_2O_3 and $BiTaO_4$ have been examined. The β-Bi_2O_3-related solid solution and the δ-Bi_2O_3-related type I and type II solid solutions are isomorphous with the analogues in the Bi_2O_3–Nb_2O_5 system. Two monoclinic structures with the compositions of $Bi_7Ta_3O_{18}$ (type II*) and $Bi_4Ta_2O_{11}$ (type III) are proposed. The composition dependence of the structure transition and the structure dependences of band gaps and thermoelectric power of the materials are discussed.

Introduction

Pure Bi_2O_3 normally exists in a monoclinic phase (α-Bi_2O_3) (*1*) at room temperature. Above 729°C, it transforms from the α-phase to a δ-phase (*2*) which has a defect fluorite structure. In addition, when cooling down the sample from high temperature, two metastable phases, tetragonal β-Bi_2O_3 (*3*) and body-centered cubic γ-Bi_2O_3 (*4*) may be obtained at 650 and 639°C, respectively. Probably the most interesting phase of pure Bi_2O_3 is the δ-type, since it is the best oxide ion conductor known (*5*), with a conductivity of ca. 1 Ω^{-1} cm^{-1} at 1023 K. Unfortunately, the δ-Bi_2O_3 phase cannot be quenched to room temperature. It is believed that the instability of the δ-Bi_2O_3 structure mainly results from oxygen vacancies (25% of the anionic sites) in the fluorite-like structure.

On the other hand, many metal oxides can be dissolved into the Bi_2O_3 structure and the high-temperature phases of Bi_2O_3 are preserved at room temperature (*6*). Several Bi_2O_3-containing ternary oxide systems, Bi_2O_3–Nb_2O_5 (*7, 8*), Bi_2O_3–V_2O_5 (*9, 10*), and Bi_2O_3–WO_3 (W. Zhou *et al.*, manuscript in preparation), have been previously investigated by using high-resolution electron microscopy (HREM). Except for the β- and γ-type solid solutions obtained in very rich Bi compositions, the δ-type solid solutions were found in the greatest compositional range in each system. The guest cations in these materials, Nb, V, and W, were in 5+ or 6+ charge valences. Therefore, some extra oxygen anions were introduced into the δ-Bi_2O_3 structure to reduce the anion vacancies. Furthermore, the ionic radii of Nb^{5+} (r = 0.69 Å), V^{5+} (0.59 Å), and W^{6+} (0.62 Å) are significantly smaller in size than Bi^{3+} (0.96 Å). According to laser Raman studies (I. E. Wachs, unpublished work), these cat-

0022-4596/92 $5.00

ions were in tetrahedral (for V^{5+}) and octahedral (for Nb^{5+} and W^{6+}) coordinations by oxygen in spite of eight anionic sites surrounding each cation in the fluorite structure and, therefore, some anion vacancies were "frozen" at room temperature. The formation of NbO_6 octahedra in the defect fluorite structure by shifting oxygen atoms was discussed in Ref. (*7*). There is no doubt that the δ-Bi_2O_3 structure can be preserved in a solid solution state. However, it was found that the real structures of the δ-type solid solutions were far more complex than we expected, even though X-ray powder diffraction (XRD) patterns from these materials seem to be identical to that from pure δ-Bi_2O_3. When the concentrations of the guest oxides were low, the guest cations existed separately in some ordered arrangements to form a $2 \times 2 \times 2$ body-centered cubic superstructure derived from the δ-Bi_2O_3 subcell in the Bi_2O_3–Nb_2O_5 system, a $3 \times 3 \times 3$ face-centered cubic superstructure in the Bi_2O_3–V_2O_5 system, and two tetragonal superstructures in the Bi_2O_3–WO_3 system. Further addition of the guest oxides resulted in various superstructures due to some ordered or partially ordered arrangements of tetrahedral clusters, Nb_4O_{18}, V_4O_{10}, and W_4O_{18}, separated by a matrix of the δ-Bi_2O_3 structure (*7–10*). In the case of the Bi_2O_3–Nb_2O_5 system, some Nb_4O_{18} tetrahedra altered into Nb_4O_{20} square clusters at the composition of $Bi_7Nb_3O_{18}$ (*8*).

The physicochemical properties of these solid solution materials were found to depend on their detailed structures (*11*). Therefore, to describe the structures of these solid solution materials, we prefer to use a multi-order approximation method, i.e., the basic structures determined by XRD are the first-order approximations and the more detailed structures revealed by electron microscopy are the second-order approximations to the true structures.

Ta- and Nb-containing compounds are usually isomorphous. For example, using the XRD technique, Bi_3TaO_7 was previously identified to be a cubic phase with $a = 5.447$ Å (*12*), similar to the basic unit cell of Bi_3NbO_7. No superstructure was observed at that stage. $BiTaO_4$ (*13*) is also isostructural with $BiNbO_4$, being orthorhombic at low temperature and triclinic at high temperature (>900°C). In a short communication, superstructures and measurement of band gaps of some solid solutions in the Bi_2O_3–Ta_2O_5 system have been reported (*14*). In this present work, the details of the structure determination by HREM, phase transition, and some physical properties of the bismuth tantalum oxides in the compositional range from Bi_2O_3 to $BiTaO_4$ are discussed. Similarities and differences between the Bi_2O_3–Nb_2O_5 and Bi_2O_3–Ta_2O_5 systems are also examined.

Experimental

Microcrystalline samples of the ternary oxides were prepared by solid state reaction of Bi_2O_3 and Ta_2O_5, both of 99.9% purity. A mixture of the oxides was ground with acetone in an agate mortar and pestle for a few minutes. The slurry was then allowed to dry in air before being placed in a silica boat. This was then placed in an electrically heated tubular furnace operating at the desired temperature (820 to 1000°C). To avoid possible reduction of the specimens, pure oxygen with a flow rate of ca. 15–20 cm^3/min at 1 atm was used during the preparations. Initial preparation times were in the range 24–182 h, with further annealing under identical conditions in cases where nonhomogeneity was subsequently found. Sintered specimens were quenched directly to room temperature. Table I shows the preparation conditions for each composition.

Initial characterization of the specimens was by XRD on a Philips diffractometer using copper $K\alpha$ radiation with operating conditions of 40 kV and 40 mA. The compositions of the specimens were examined by

TABLE I

LIST OF SPECIMEN PREPARATIONS WITH STARTING COMPOSITION, HEATING TEMPERATURE, INITIAL HEATING TIME, AND PHASES PRESENT

Starting composition (Bi_2O_3 : Ta_2O_5)	Heating temperature (°C)	Initial time (hr)	Main phases present (type)
60 : 1	820	182	β
39 : 1	825	148	β
25 : 1	820	182	β, I
19 : 1	825	168	I
15 : 1	825	110	I
9 : 1	825	110	I, II
4 : 1	825	148	II
3 : 1	825	78	II, II*
7 : 3	1000	24	II*
2 : 1	1000	24	III
5 : 3	1000	50	IV, $BiTaO_4$
1 : 1	1000	50	$BiTaO_4$

energy dispersive X-ray spectrometry (EDS) on a Jeol JEM-200CX electron microscope. Freshly prepared monophasic Bi TaO_4 was used as reference material in the EDS studies. Final structure determination was by analysis of selected area electron diffraction (SAED) patterns and HREM images; the latter were taken from another Jeol JEM-200CX electron microscope, in which a new specimen stage was used with C_c = 1.05 mm, C_s = 0.52 mm and an absolute information limit ca. 1.8 Å. Computer image simulation was according to the multislice method (*15*), using a special program developed for very large unit cells (*16*). The phases presented in each specimen are listed in Table I. The measurements of band gap and thermoelectric power were performed in the Royal Institution in London and University of Kent at Canterbury, respectively. The experimental details were the same as those for the Bi_2O_3–Nb_2O_5 system (*11*, *17*).

Results and Discussion

Similar to those of the Bi_2O_3–Nb_2O_5 system, the XRD patterns (Fig. 1) from the specimens prepared exhibited only several basic structures. The unindexed weak peaks in the XRD spectra of 60 : 1, 25 : 1, and 19 : 1 were from an impurity of α-Bi_2O_3. A δ-Bi_2O_3-like structure was found to cover a wide range of compositions (19 : 1 to 3 : 1). Some weak peaks also presented in the XRD spectra of 9 : 1, 4 : 1, and 3 : 1 and did not vanish at high temperature (>750°C), indicating existence of superstructures. But it was difficult to index these weak peaks. A laser Raman study (I. E. Wachs, unpublished work) indicated that, in all the samples, Ta cations were in an octahedral coordination by oxygen. HREM studies were then carried out to ascertain if there were

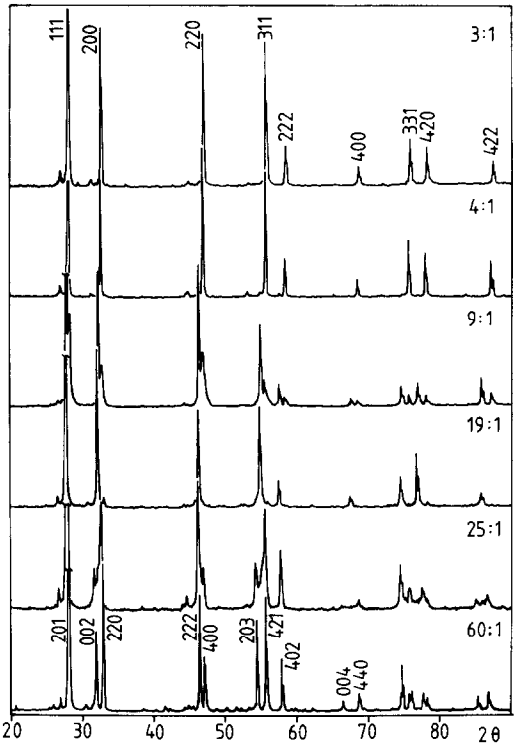

FIG. 1. XRD spectra of some compositions in the Bi_2O_3–Ta_2O_5 system, the cation ratio Bi : Ta being indicated. In the 3 : 1 case, the observed lines are accorded indices on the conventional fluorite unit cell. The reflection peaks from 60 : 1 are indexed onto a β-Bi_2O_3-like unit cell.

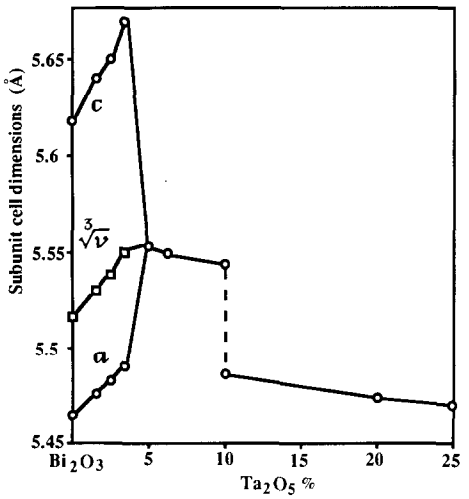

FIG. 2. Composition dependence of the fluorite-like subunit cell parameters of the β-type, type I, and type II structures in the Bi_2O_3–Ta_2O_5 system.

ordered arrangements of cations and, therefore, superstructures.

β-Bi_2O_3-like Structure

From $Bi_{60}TaO_{92.5}$, a β-Bi_2O_3-like phase, being tetragonal with $a \approx 7.74$ and $c \approx 5.63$ Å, was stabilized at room temperature until the composition reached $Bi_{25}TaO_{40}$, where the structure started to transform to a cubic phase (Fig. 1). This β-type range was narrower than that in the Bi_2O_3–Nb_2O_5 system, where $Bi_{25}NbO_{40}$ was clearly a homogeneous β-type. The unit cell parameters of this β-type solid solution structure continuously increased with the doping of Ta_2O_5 (Fig. 2). Bearing in mind that the cation Ta^{5+} (r = 0.68 Å) is much smaller in size than Bi^{3+} (r = 0.96 Å), this composition dependence of unit cell parameters can be explained as follows. The β-Bi_2O_3 structure can be considered as a $\sqrt{2} \times \sqrt{2} \times 1$ superstructure based on δ-Bi_2O_3 due to cation displacement toward anion vacancies, the unit cell being actually compressed. When Ta_2O_5 was added, some vacancies were filled by oxygen and the atomic displacement was reduced. As a result, the lattice constant increased. The β-Bi_2O_3-like structure was authenticated by SAED patterns and HREM images (Figs. 3a and 3d).

The β-Bi_2O_3 structure did not present ion conductivity except at high temperature when it had transformed to the δ-phase. However, an interesting property was observed, i.e., its thermoelectric power was sensitive to oxygen pressure. Thermoelectric power of solid solution material $Bi_{60}NbO_{92.5}$ has been measured previously (*17*). At high temperature (1033 K), the δ-phase specimen showed anionic conducting property and its thermoelectric power was less sensitive to oxygen pressure. But, at low temperature (768 K), when the specimen was in the β-phase, the thermoelectric power exhibited very high sensitivity to oxygen pressure. Ta-doped β-Bi_2O_3 presented a similar property. Figure 4 shows the dependence of thermoelectric power ($-\theta$) on oxygen pressure ($\ln P_O$) in $Bi_{39}TaO_{61}$. At low oxygen pressure, the θ value was even more sensitive to pressure. However, unlike the results from the Nb-doped β-Bi_2O_3 phase (*17*), the relation between the $-\theta$ and $\ln P_O$ was not linear and the temperature effect was obvious in this system (Fig. 4). The pretreatment of the specimen was the same as that for the Nb-doped sample as described in Ref. (*17*). The origin of this pressure dependence of thermoelectric power in the β-Bi_2O_3-related solid solutions and the difference on this property between the Nb-doped and Ta-doped specimens are still unknown.

Another remarkable physical property of the β-Bi_2O_3 solid solution is its low band gap (*14*). Although the band gaps for pure Bi_2O_3 (α-type) and Ta_2O_5 at room temperature are 2.77 and 3.32 eV, respectively, the solid solution of Ta-doped β-Bi_2O_3 has a band gap about 2.2 eV (Fig. 5). According to an optical absorption study, pure β-Bi_2O_3 should demonstrate an absorption edge at about 2.6

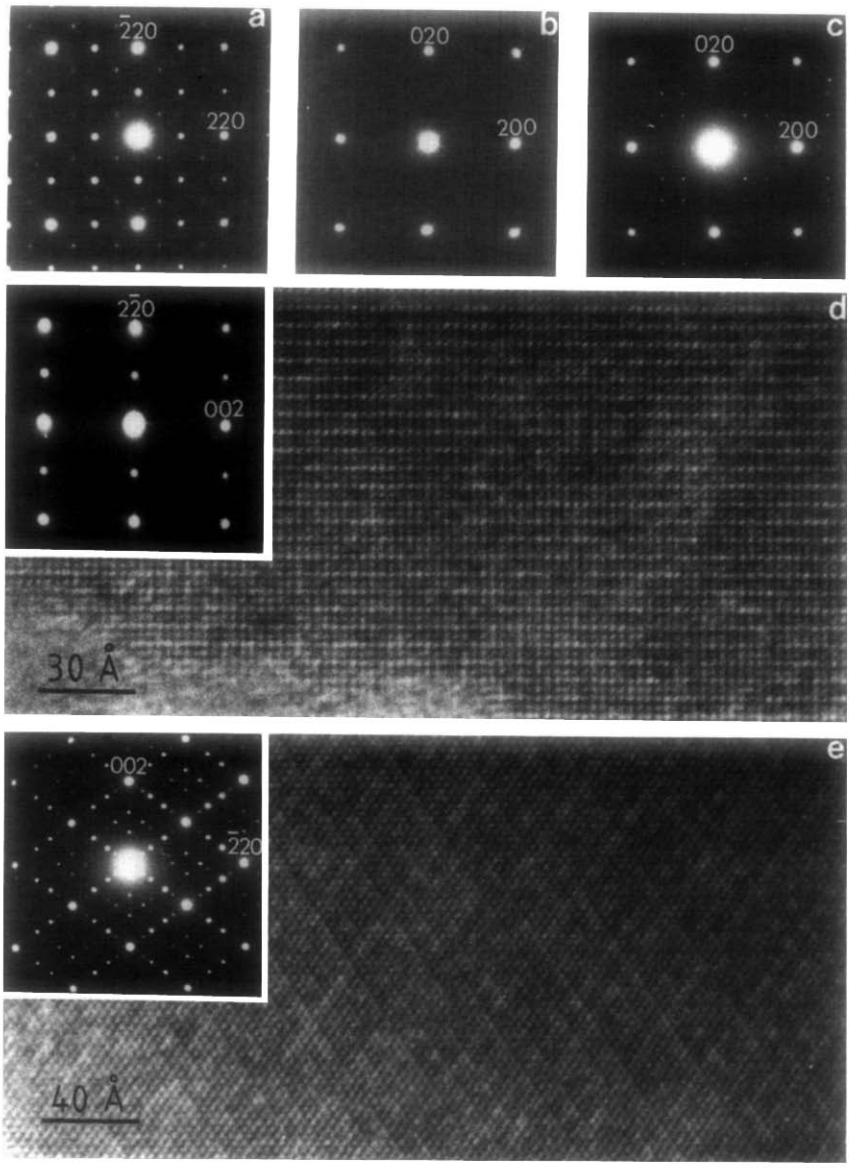

FIG. 3. SAED patterns on the [001] projections of the β-type structure from $Bi_{39}TaO_{61}$ (a), the type I structure from $Bi_{19}TaO_{31}$ (b), and the type II structure from $Bi_8Ta_2O_{17}$ (c). HREM images viewed down the [110] directions of the β-type (d) and the type II structures (e). Maxima corresponding to the β-Bi_2O_3 unit cell (a, d) and the fluorite subunit cell (b, c, e) are indexed.

eV (*18*) and the band gap of pure δ-Bi_2O_3 is in a 0.5–1 eV infrared range (*19*). The reduction of band gap in Ta-doped β-Bi_2O_3 supports that the β-type solid solution has an intermediate structure between pure β-Bi_2O_3 and δ-Bi_2O_3 in terms of the lattice symmetry and the metal–oxygen bonding distances.

Type I Structure

When the composition fell into the range from $Bi_{19}TaO_{31}$ to Bi_3TaO_7, some cubic phases appeared and the observed XRD spectra matched the δ-Bi_2O_3 structure (Fig. 1). At the composition of Bi_9TaO_{16}, all reflection lines split into doublets, which indicated two similar cubic substructures. SAED patterns and HREM images indicated that the first cubic phase (type I) existed in the nominal compositional range from $Bi_{19}TaO_{31}$ to Bi_9TaO_{16} (Fig. 3b). From many SAED patterns and HREM images, it was confirmed that this type I structure was isomorphous to the analogue in the Bi_2O_3–Nb_2O_5 system (*7*). The unit cell of a typical type I structure had a composition of $Bi_{30}Ta_2O_{50}$ and was a body-centered cubic $2 \times 2 \times 2$ superstructure derived from δ-Bi_2O_3. The lattice constant, a, was about

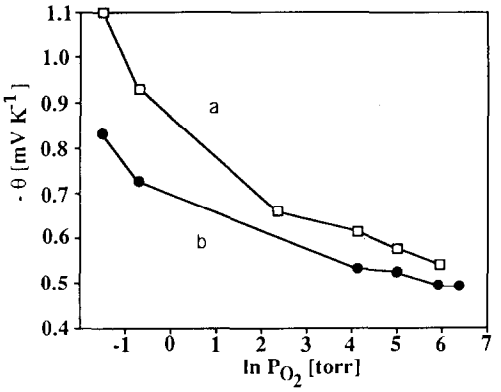

FIG. 4. The dependence of thermoelectric power θ on oxygen pressure in $Bi_{39}TaO_{61}$ at temperatures of 753 K (a) and 848 K (b).

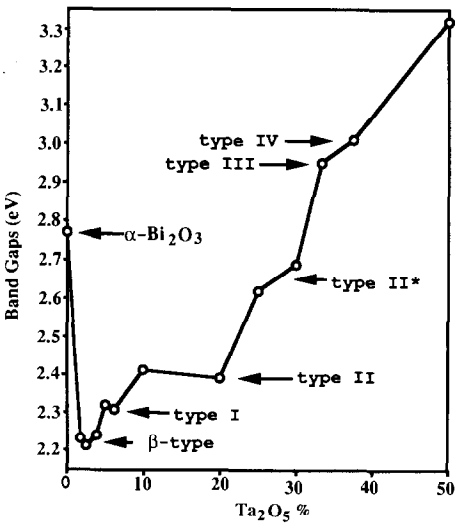

FIG. 5. Band gap measurement for the solid solution materials in the Bi_2O_3–Ta_2O_5 system. The different superstructures are indicated.

11.1 Å. Although the HREM images provided insufficient contrast for understanding the exact atomic arrangement in the type I superstructure, according to the composition and the symmetry of the structure, also confirmed by a refinement of the SAED patterns, the most possible modification for the type I structure was suggested to be replacing two Bi cations at the corner and the body-center of the unit cell by Ta cations (Fig. 6a). When the composition contained less Ta, the Bi cations on these two sites were only partially substituted by Ta. The SAED patterns of the cubic phase from the $Bi_{25}TaO_{40}$ and $Bi_{19}TaO_{31}$ nominal compositions were identical to those from $Bi_{30}Ta_2O_{50}$. The intensities of the satellite spots on the SAED patterns from $Bi_{30}Ta_2O_{50}$ were much weaker compared with those from $Bi_{30}Nb_2O_{50}$. This supported that, unlike the β-type solid solution, the type I superstructure was predominantly based on an ordering of cations rather than lattice distortion. The lattice dimension was, therefore, simply decreased with the Ta_2O_5-doping (Fig. 2).

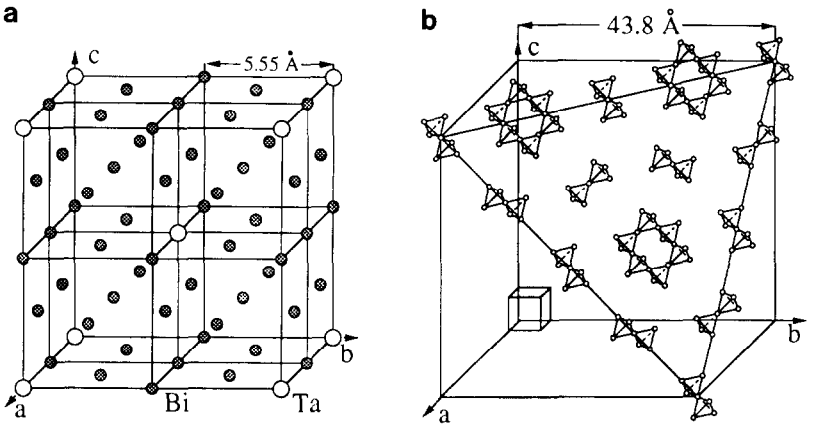

FIG. 6. The structural models for the type I (a) and type II (b) in the Bi_2O_3–Ta_2O_5 system. Only cations are shown in (a); (b) shows the arrangement of Ta–O clusters on one of the four (111) planes, only Ta cations being presented. The small cubes represent the fluorite-like subceli.

It was assumed that when the Ta concentration was increased, Bi cations were more or less oxidized and Bi–O bond lengths decreased, moving the Bi 6*p* band down. Therefore, the band gap of the type I phase was higher than that of the β-type phase (Fig. 5) in spite of the higher symmetric δ-phase structure.

When the concentration of Ta_2O_5 in the solid solution increased from $Bi_{30}Ta_2O_{50}$, TaO_6 octahedra were impossible to be isolated and a Ta–O–Ta chemical bond must have occurred, giving rise to some more complex structures.

Type II Structure

The type II structure was also isomorphous to the analogue in the Bi_2O_3–Nb_2O_5 system and covered a nominal compositional range from Bi_9TaO_{16} to Bi_3TaO_7. The SAED patterns and HREM images obtained from any composition in this range were very similar (Figs. 3c and 3e). But the positions and intensities of the satellite spots on the SAED patterns derived from the superstructures were variable, indicating an incommensurate state. However, to facilitate understanding of the structure, an ideal model has been chosen for the type II structure, which has an $8 \times 8 \times 8$ superunit cell based on δ-Bi_2O_3 in a space group of $Fd3m$. The lattice constant, a, becomes 43.8 Å. The composition of the whole unit cell is $Bi_{1648}Ta_{400}O_{3472}$. Ta cations are in two kinds of clusters, Ta_7O_{30} and $Ta_{18}O_{72}$. Those in the Ta_7O_{30} group are located at (16*c*) and (96*g*) *m* (*xxz* = 1/16, 1/16, 2/16) and those in the $Ta_{18}O_{72}$ group at (96*g*)*m* (*xxz* = 1/16, 1/16, 12/16), (96*g*) *m* (*xxz* = 1/8, 1/8, 1/2), and (96*h*) 2 (x = 5/16). The arrangement of Ta cations on one of the four (111) planes in the type II superstructure is shown in Fig. 6b, which is identical to the ideal model for the type II structure in the Bi_2O_3–Nb_2O_5 system (*7*). The latter has been confirmed by computer image simulation (*7*) and also by computer simulation of SAED patterns (D. Tang, unpublished work).

It is interesting that, when the concentration of Ta was high enough to form some Ta–O clusters, Ta_2O_x and Ta_3O_x clusters were unlikely to exist inside the δ-Bi_2O_3 structure. Ta cations with oxygen directly

formed Ta_4O_{18} tetrahedral clusters, constructed from four TaO_6 octahedra. These clusters joined together to form larger ones, Ta_7O_{30} and $Ta_{18}O_{72}$, lying on all four (111) planes of the type II unit cell. Nevertheless, the Ta_4O_{18} tetrahedron was still the most characteristic figure of the type II superstructure. We designated such clusters pyrochlore-like units (*7*) because a complete three-dimensional network of such an arrangement for tantalum oxide with a matrix of bismuth oxide would lead to a hypothetical pyrochlore structure with a composition of $Bi_2Ta_2O_7$, which was never practically observed.

Because the type II superstructure, like the type I structure, mainly resulted from an ordering of the cations, the sublattice constant simply decreased with the doping of Ta_2O_5, due to the different cationic radii between Bi^{3+} and Ta^{5+}. However, the basic unit cell dimensions of the type I and type II structures were significantly different (Fig. 2), which was not observed in the Bi_2O_3–Nb_2O_5 system.

The band gap of the type II phase further increased (compared to the β-type and type I phases) as we expected and depended on the detailed structure, rather than the composition (Fig. 5).

It was obvious that the XRD result from the specimen of Bi_3TaO_7 (Fig. 1) indicated a fluorite-like cubic phase with a = 5.45 Å, which was very similar to the XRD pattern from $Bi_8Ta_2O_{17}$ and in good agreement with the previous report (*12*). The majority phase was indeed close to Bi_3TaO_7, which was confirmed by EDS, and had the type II structure revealed by the SAED and HREM studies. However, a minority phase with a composition of $Bi_7Ta_3O_{18}$, which was found to have a monoclinic structure, was also detected.

There must be an upper limit of composition for the type II structure. If the structural model (Fig. 6b) supported by computer image simulation is acceptable, each Ta_7O_{30} cluster freezes eight oxygen vacancies and each $Ta_{18}O_{72}$ cluster freezes 18 oxygen vacancies in the defect fluorite structure and the numbers of these two clusters are the same. This means 25 Ta atoms will freeze 26 oxygen vacancies. We suppose there are no other oxygen vacancies inside the structure when the composition reaches the upper limit, and the general composition of the ternary oxide becomes $Bi_2Ta_xO_{3+2.5x}$, with $1–0.5x$ oxygen vacancies. Therefore, to maintain the type II structure, $x < 0.649$ and the upper composition limit of the type II structure is about $Bi_3Ta_{0.97}O_{6.925}$, which is in very good agreement with the experimental results. Further addition of Ta_2O_5 into this composition must give rise to some new phases.

Type II Structure*

To prepare a monophasic specimen of the new compound found in the Bi_3TaO_7 specimen, a nominal composition of $Bi_7Ta_3O_{18}$ was first heated at 825°C for 24 hr. The XRD spectrum, comprising a type II-like cubic pattern with many unindexed diffraction peaks, indicated a multiphasic state. The sample was then reheated at 1000°C for 24 hr and at 1100°C for another 6 hr followed by quenching to room temperature. The cubic phase disappeared from the XRD spectrum (Fig. 7) and the final specimen exhibited no change under further annealing. The homogeneity of the sample was confirmed by EDS.

Although the XRD spectrum of $Bi_7Ta_3O_{18}$ was very complicated and was significantly different than that of the type II structure, the SAED patterns revealed a strongly relationship between the type II and the new phase, designated type II*. Figure 8a and 8d are SAED patterns of the incommensurate type II structure from $Bi_8Ta_2O_{17}$. Figures 8b and 8e were obtained from the specimen of $Bi_7Ta_3O_{18}$ after being heated at 825°C for 24 hr. The relative intensities of the original spots of the type

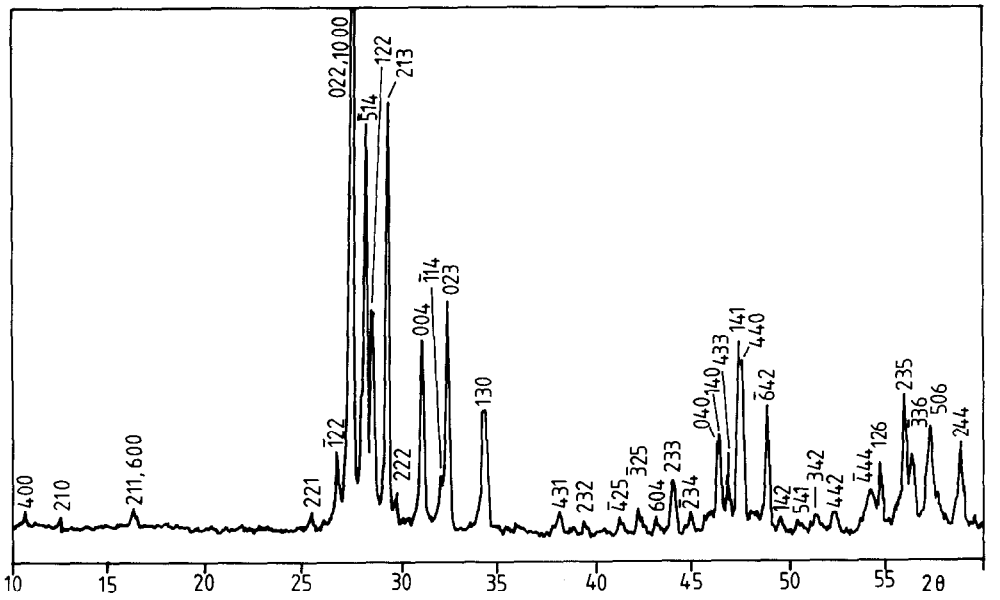

FIG. 7. XRD spectrum of $Bi_7Ta_3O_{18}$ indexed onto a monoclinic unit cell with a = 38.5, b = 7.7, and c = 13.64 Å and β = 124.33°.

II structure were altered, but the diffraction patterns from the basic fluorite substructure remained. Figures 8c and 8f, recorded from the final sample of $Bi_7Ta_3O_{18}$ after annealing at 1100°C for 6 hr, show the SAED patterns of type II*. Comparing these SAED patterns, three main suggestions can be made. First, the substructure of the type II* is still fluorite-like with significant lattice distortion. The relation between the superlattice and the fluorite-like sublattice is represented as

$$\mathbf{a}_{II^*} = 5\mathbf{a}_f - 5\mathbf{b}_f,$$

$$\mathbf{b}_{II^*} = \mathbf{a}_f + \mathbf{b}_f,$$

$$\mathbf{c}_{II^*} = \mathbf{a}_f + \mathbf{b}_f + 2\mathbf{c}_f,$$

where **a**, **b**, and **c** are unit cell vectors. Second, there might also be some pyrochlore-like Ta_4O_{18} tetrahedral clusters in the type II* structure. These clusters lie on only one (111) plane of the fluorite structure instead of all four (111) planes in type II. The ordering along the [111] direction of the fluorite-like subcell is commensurate and fivefold. Third, the phase transition from type II to type II* is gradual, suggesting that there is no boundary between the two phases. By tilting the specimen stage, a series of SAED patterns were obtained from one single microcrystal of $Bi_7Ta_3O_{18}$. The unit cell was therefore determined to be monoclinic with a = 38.5, b = 7.70, c = 13.64 Å, and β = 124.33°. Using these unit cell parameters, the XRD spectrum of Fig. 7 was indexed. However, to refine the XRD spectrum using such a large unit cell is extremely difficult. Alternatively, HREM technique was applied to study the detailed type II* structure. One principal HREM image viewed down the [010] projection of the type II* unit cell is shown in Fig. 9. Superstructure ordering in one of the ⟨111⟩ directions of the fluorite subcell can be apparently observed.

Note that in the previous work in these laboratories, a type II family of Bi–V–O

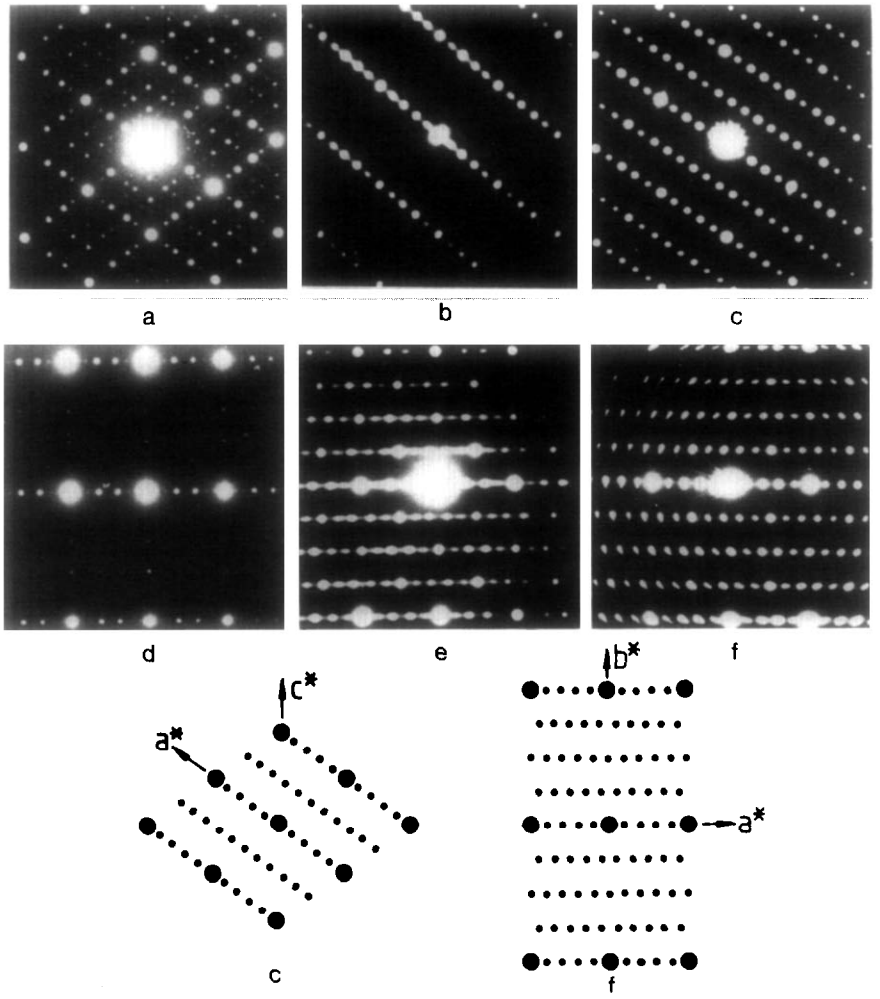

FIG. 8. SAED patterns viewed down the [110] (a, b, c) and [112] (d, e, f) projections of the fluorite-like subcell, showing the phase transition from the type II to type II* structures. (a) and (d) were obtained from $Bi_8Ta_2O_{17}$; (b) and (e) from $Bi_7Ta_3O_{18}$, after heating at 825°C for 24 hr; (c) and (f) from $Bi_7Ta_3O_{18}$ after reheating at 1100°C for 6 hr. The monoclinic unit cell axes of type II* are indicated on the schematic drawings of (c) and (f).

ternary oxides was found, in which VO_4 tetrahedra lay down one of the {111} planes of the defect fluorite structure to form series of monoclinic structures (*9, 10*). Both of the SAED patterns and the HREM image of the type II* $Bi_7Ta_3O_{18}$ structure in Fig. 8 and Fig. 9 are very similar to those of the type II phases in the Bi_2O_3–V_2O_5 system, except that, in the Bi_2O_3–V_2O_5 system, the multiplications of diffraction spots on the SAED patterns along the main [111] direction of the fluorite subcell are 6, 8, or 24, while in $Bi_7Ta_3O_{18}$, only a fivefold repeat was observed. Using the structural principle for the type II Bi–V–O, some Ta_4O_{18} tetrahedral units were placed on one (111) plane of the fluorite structure. However, such an arrangement never reproduced the details of

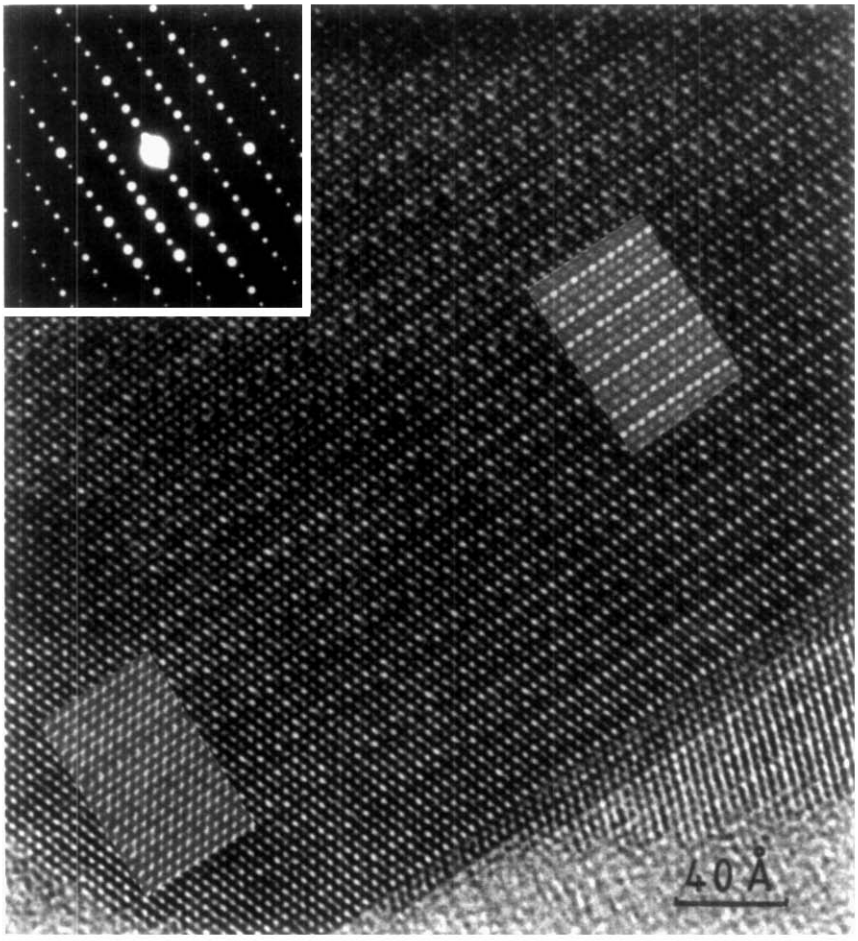

FIG. 9. HREM image of the type II* structure with the composition of $Bi_7Ta_3O_{18}$, viewed down the [010] direction. The insets show computer-simulated images using the model of Fig. 10 with specimen thicknesses of 80 Å (left) and 120 Å (right) and lens defocuses of 850 Å (left) and 650 Å (right).

the HREM image shown in Fig. 9. It is necessary to have some separate Ta cations substituting Bi in the space between these planes. After testing more than 10 models, the final model for $Bi_7Ta_3O_{18}$ is shown in Fig. 10. A computer image simulation showed that the image contrast with different thicknesses from the type II* structure can be reproduced from this model, shown by the insets of Fig. 9. It has been noted that the right bottom area of Fig. 9 shows the type II* structure intergrowing with a new phase in a twin-like manner. The latter, being a threefold superstructure along the [111] direction of the fluorite subcell, was confirmed to be a type III structure described in next section.

The composition of the type II* model shown in Fig. 10 is exactly $Bi_7Ta_3O_{18}$ or $Bi_{56}Ta_{24}O_{144+16\Delta}$ for a unit cell, where Δ stands for oxygen vacancies. All 16 oxygen vacancies surround the Ta_4O_{18} clusters. Although those isolated Ta cations are still in octahedral coordination with oxygen as indicated

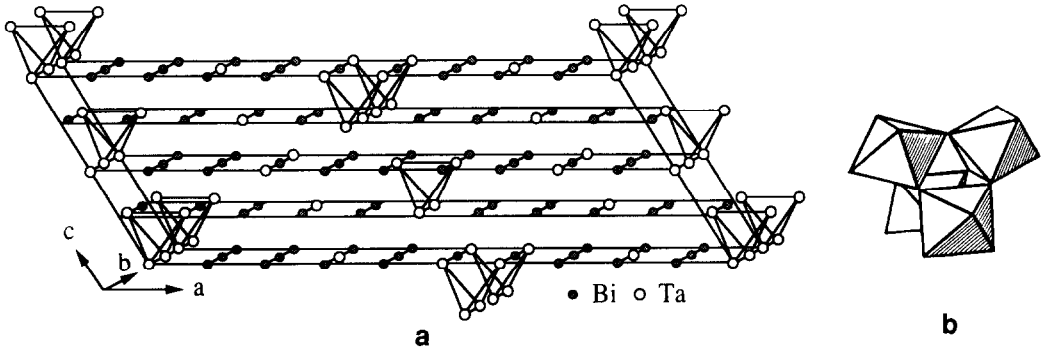

FIG. 10. (a) Suggested model for the type II* structure with the composition of $Bi_7Ta_3O_{18}$. Only cations are shown. (b) A Ta_4O_{18} tetrahedral unit.

by laser Raman studies, two other anionic sites around these guest cations might be also occupied by oxygen with significantly longer Ta–O bond lengths. The lattice, of course, must be distorted as we observed in the XRD pattern (Fig. 7). Therefore, the reason for the phase transition from the type II to the type II* is the extra oxygen atoms occupy the anion vacancies surrounding the Ta_4O_{18} clusters and break up some of these tetrahedral clusters. But it is still unknown why the remaining Ta_4O_{18} tetrahedra lie on only one (111) plane to form a monoclinic superstructure instead of a tetragonal phase as the type III structure in the Bi_2O_3–Nb_2O_5 system (*8*). With the lattice distortion from a cubic symmetry, the band gap of the type II* phase increases substantially compared with the value for the type II phase (Fig. 5).

Type III Structure

When the starting composition of $Bi_4Ta_2O_{11}$ was heated at 825°C for 24 hr, the XRD spectrum was very similar to that of the $Bi_7Ta_3O_{18}$ composition. However, when the specimen was reheated at 1000°C for another 24 hr, some new phases were produced. Further heating at 1100°C for 6 hr, the XRD spectrum of the sample was similar to that of $Bi_5Ta_3O_{15}$, which had an Aurivillius-related structure (type IV) (*20*). It was strongly supported by the HREM studies that at least one new phase, designated type III, existed between the type II* and type IV structures. Although it might not be a dynamically stable phase since the XRD spectra always indicated a multiphasic state, the new phase would give some information about the phase transition from type II to type IV. According to a series of SAED patterns from one single microcrystal, the unit cell of the type III structure was determined to be monoclinic with a = 24.14, b = 14.63, c = 13.47 Å, and β = 126.2°. Two principal HREM images and the corresponding SAED patterns of the type III structure are shown in Fig. 11. A threefold superstructure derived from the fluorite-like substructure in the [111] direction instead of a fivefold in the type II* structure was easily observed from the image of Fig. 11a. The image contrast of Fig. 11a is identical to that of the right bottom area of the image in Fig. 9, suggesting that both images present the same phase. Since the type III phase is derived from the type II* phase and it can intergrow with the type II*, it is assumed that the new structure is still related to the fluorite structure. According to the intensities of diffraction spots of the SAED patterns, the relation between the superlattice

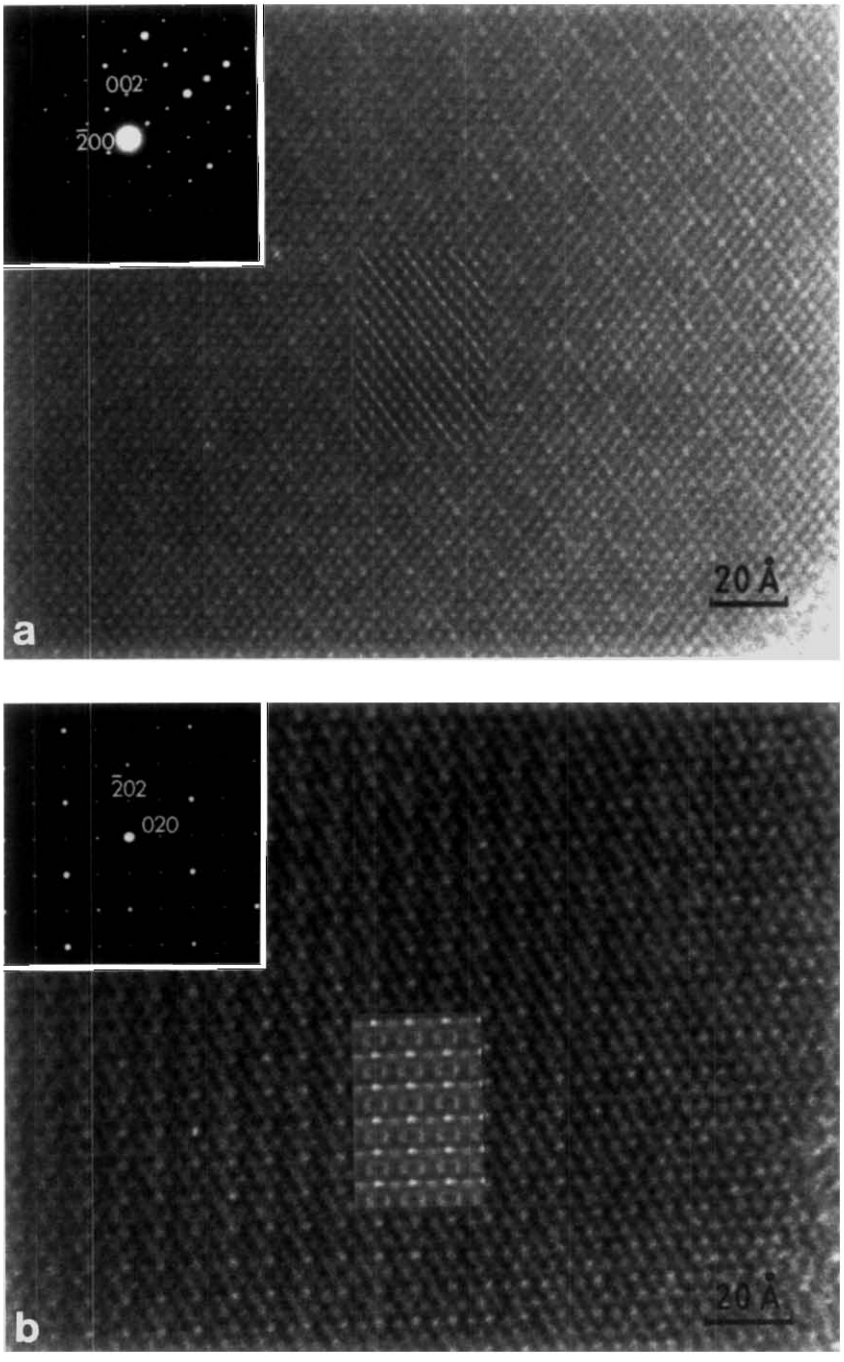

FIG. 11. HREM images of the type III structure viewed down the [010] (a) and the [101] (b) directions. The insets show the computation images from a model shown in Fig. 12 with the conditions of (a) 20 Å specimen thickness, 1600 Å defocus and (b) 40 Å specimen thickness, 800 Å defocus.

and the fluorite-like sublattice can be represented by

$$\mathbf{a}_{III} = 3\mathbf{a}_f - 3\mathbf{b}_f,$$

$$\mathbf{b}_{III} = 2\mathbf{a}_f + 2\mathbf{b}_f,$$

$$\mathbf{c}_{III} = -\mathbf{a}_f + \mathbf{b}_f + 2\mathbf{c}_f.$$

Comparing the unit cells of type II* and type III, it is obvious that all three unit cell axes in both phases orient to the same directions in the δ-Bi_2O_3 reference sublattice, that the **c** dimensions are identical, and that the **b** dimension of the type III phase is simply a doubling of the **b** dimension of the type II* phase. Consequently, it is not surprising to see on Fig. 9 that the interface where the type II* and type III structures intergrow together is the (*bc*) plane for both phases. In other words, the (*bc*) planes in both of the real unit cells or the main (111) planes of the fluorite-like subunit cells, on which the Ta_4O_{18} units lie, have a strong similarity.

Suppose the structure principle of type III in the titled system is similar to that in the Bi_2O_3–Nb_2O_5 system (*8*), when the content of Ta_2O_5 increases from the upper composition limit of the type II structure, some pyrochlore-like Ta_4O_{18} tetrahedra units in the type II structure will be rearranged into perovskite-like Ta_4O_{20} square units. Bearing in mind that the type III structure of $Bi_4Ta_2O_{11}$ is derived from the monoclinic type II* structure, the intergrowth of the pyrochlore-like Ta_4O_{18} units and the perovskite-like Ta_4O_{20} units will not extend in three dimensions but only in one dimension. One possible model for the type III structure is shown in Fig. 12. The simulated images from this model can reproduce the details of the observed image contrasts in two directions (Fig. 11). It is then deduced that the type III structure forms when the concentration of Ta in the type II* structure increases, some of the Ta_4O_{18} tetrahedral units being rearranged into Ta_4O_{20} perovskite-like units to accommodate more oxygen ions and to link with the rest in the **a** direction.

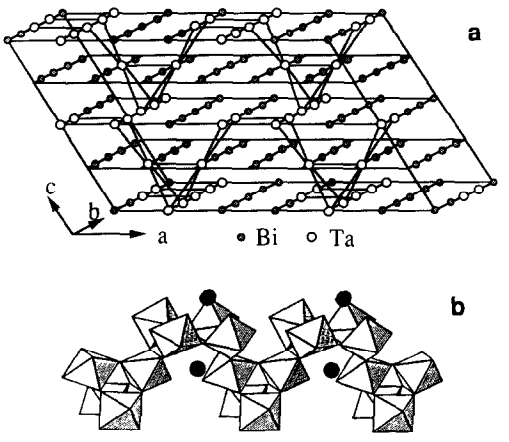

FIG. 12. (a) Suggested model for the type III structure with the composition of $Bi_4Ta_2O_{11}$. Only cations are shown. (b) A model of regular intergrowth of the Ta_4O_{18} and Ta_4O_{20} units.

Comparing two type III structures in the Bi_2O_3–Nb_2O_5 (*8*) and Bi_2O_3–Ta_2O_5 systems, it is recognized that the structural principles of these phases are very similar, i.e., the network of MO_6 (M = Nb, Ta) octahedra are built up by regular 1 : 1 intergrowth of the perovskite-like M_4O_{20} units and the pyrochlore-like M_4O_{18} units. Such an intergrowth is only one-dimensional along the **a** direction to form a monoclinic unit cell in the Ta-doped type III phase instead of three-dimensional, forming a tetragonal unit cell in the Nb-doped type III phase. Unlike $Bi_7Nb_3O_{18}$, both the type II* $Bi_7Ta_3O_{18}$ and the type III $Bi_4Ta_2O_{11}$ are metastable phases found in a phase transition process from the type II to the type IV structures. There may be more than two intermediate phases and it is difficult to identify the phase boundaries in this compositional range. Furthermore, the models in Fig. 10 and Fig. 12 display only the most possible cation arrangements for the type II* and type III structures. The exact atomic coordinates (especially for oxygen) cannot be determined at this stage. However, they show structural principles and close approximations to the type II* and

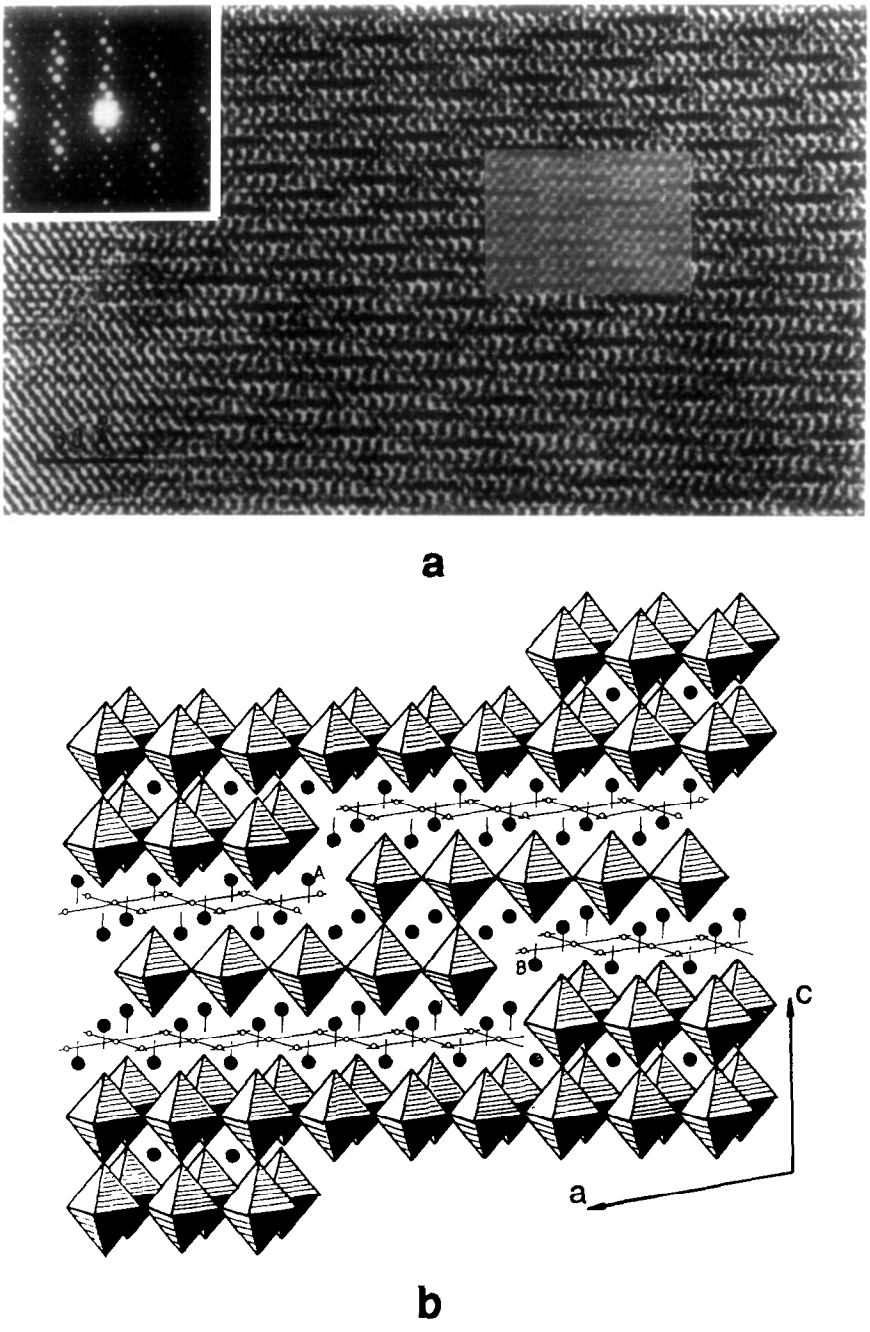

FIG. 13. HREM image viewed down the [010] direction (a) and the proposed structural model (b) of the type IV structure with a composition of $Bi_{31}Ta_{17}O_{89}$. The insets of (a) are the corresponding SAED pattern (left) and a computer-simulated image from the model (b) at the conditions of 80 Å specimen thickness and 400 Å lens defocus (right).

type III structures compared with the XRD results and are helpful in understanding the phase transition in this ternary oxide system.

Type IV Structure

When the content of Ta_2O_5 further increased, all the pyrochlore-like units were rearranged into perovskite-like sheet components to form a type IV superstructure with a composition of $Bi_{31}Ta_{17}O_{89}$. Structure determination of the type IV phase was described in Ref. (*20*). It has a monoclinic structure with $a = 22.72$, $b = 3.85$, $c = 19.26$ Å, and $\beta = 101.9°$ and is a stepped superstructure based on a regular intergrowth of $n = 1$ and $n = 2$ members of Aurivillius family (*21*). Figure 13 shows an HREM image viewed down the [010] direction and an ideal model of $Bi_{31}Ta_{17}O_{89}$. There are two type IV structures observed on $Bi_5Nb_3O_{15}$, both related to the $n = 1$ and $n = 2$ Aurivillius phases (*20*). However, the stepped intergrowth in $Bi_5Nb_3O_{15}$ are along the [110] direction and, in $Bi_3Ta_{17}O_{89}$, along the [100] direction of the basic Aurivillius lattice. It is reasonable because the type IV $Bi_{31}Ta_{17}O_{89}$ is derived from the monoclinic type III $Bi_4Ta_2O_{11}$ by extending the perovskite-like Ta–O sheet components forward in the **a** direction.

$BiTaO_4$ Structure

Specimens prepared with nominal compositions between $Bi_5Nb_3O_{15}$ and $BiTaO_4$ were always mixtures of the type IV phase ($Bi_{31}Ta_{17}O_{89}$) and $BiTaO_4$. For preparation of $BiTaO_4$, several calcining temperatures were used. Up to 1000°C, a single phase of $BiTaO_4$ appeared. Below this temperature, the type IV phase always existed and its concentration decreased with the increase in temperature. All the XRD, SAED, and HREM results from the freshly prepared Bi TaO_4 agreed with the previous report (*13*). It is triclinic, containing sheets of TaO_6 octahedra parallel to the (ab) plane. Each octahedron is joined by corners to four others and the sheets are held together by Bi atoms. It was, therefore, proposed that when Ta_2O_5 was further added into the type IV structure, the perovskite-like Ta_4O_{20} units extended on the (*ab*) plane across the whole crystal to form single TaO_6 sheets which were sandwiched by Bi cations.

Conclusion

Bi-containing ternary oxides in the Bi_2O_3–Ta_2O_5 system were synthesized and investigated by HREM. Although most of the solid solutions studied are fluorite-like, their real structures can be divided into several types. TaO_6 octahedra exist separately in the β-Bi_2O_3 and type I solid solutions, but form pyrochlore-like Ta_4O_{18} tetrahedral clusters in the type II and type II* structures. Fifty percent of the Ta_4O_{18} clusters are rearranged into perovskite-like Ta_4O_{20} square clusters and regularly intergrow with the rest in the type III structure. All TaO_6 octahedra are in perovskite-like square units by sharing corners in the type IV and Bi TaO_4 phases. Consequently, very different fluorite, pyrochlore, and perovskite structural units can intergrow together and transform to each other in a doped δ-Bi_2O_3. It is believed that oxygen vacancies in the materials play an important role in these phase transitions.

Acknowledgments

The author expresses his thanks to Professor J. M. Thomas and Dr. D. A. Jefferson for helpful discussions.

References

1. M. Tsubaki and K. Koto, *Mater. Res. Bull.* **19** 1613 (1984).
2. R. S. Roth and J. L. Waring, *J. Res. Nat. Bur. Stand. Sect. A* **66A**(6), 451 (1962).
3. G. Gattow and D. Schutze, *Z. Anorg. Allg. Chem.* **328**, 44 (1964).

4. H. A. HARWIG, *Z. Anorg. Allg. Chem.* **444,** 151 (1978).
5. T. TAKAHASHI AND H. IWAHARA, *Mater. Res. Bull.*, **13,** 1447 (1978).
6. E. M. LEVIN AND R. S. ROTH, *J. Res. Nat. Bur. Stand. Sect. A* **68**(2), 197 (1964).
7. W. ZHOU, D. A. JEFFERSON, AND J. M. THOMAS, *Proc. R. Soc. London, Ser. A* **406,** 173 (1986).
8. W. ZHOU, D. A. JEFFERSON, AND J. M. THOMAS, *J. Solid State Chem.* **70,** 129 (1987).
9. W. ZHOU, *J. Solid State Chem.* **76,** 290 (1988).
10. W. ZHOU, *J. Solid State Chem.* **87,** 44 (1990).
11. A. HARRIMAN, J. M. THOMAS, W. ZHOU, AND D. A. JEFFERSON, *J. Solid State Chem.* **72,** 126 (1988).
12. E. T. SHUVAEVA AND E. G. FESENKO, *Kristallografiya* **25**(2), 408 (1980).
13. R. S. ROTH AND J. L. WARING, *Am. Miner.* **48,** 1348 (1963).
14. W. ZHOU, *Adv. Mater.* **2,** 414 (1990).
15. (a) J. M. COWLEY AND A. F. MOODIE, *Acta. Crystallogr.* **16,** 609 (1957); (b) P. GOODMAN AND A. F. MOODIE, *Acta. Crystallogr., Sect. A* **30,** 280 (1974).
16. D. A. JEFFERSON, G. R. MILLWARD, AND J. M. THOMAS, *Acta. Crystallogr., Sect. A* **32,** 823 (1976).
17. A. V. CHADWICK, W. ZHOU, AND J. M. THOMAS, *Angew. Chem. Int. Ed. Engl.* **28**(1), 75 (1989).
18. V. DOLOCAN AND F. IOVA, *Phys. Status. Solidi A* **64,** 755 (1981).
19. A. B. ANDERSON, Y. KIM, D. W. EWING, R. K. GRASSELLI, AND M. TENHOVER, *Surf. Sci.* **134,** 237 (1983).
20. W. ZHOU, D. A. JEFFERSON, AND J. M. THOMAS, *in* "Perovskite: A Structure of Great Interest to Geophysics and Materials Science" (A. Navrotsky and D. J. Weidner, Eds.), Geophys. Monograph, Vol. 45, p. 113, American Geophysical Union, Washington, DC (1989).
21. J. GOPALAKRISHNAN, A. RAMANAN, C. N. R. RAO, D. A. JEFFERSON, AND D. J. SMITH, *J. Solid State Chem.* **55,** 101 (1984).